3D-printed bioactive ceramic scaffolds with MoSe$_2$ nanocrystals as photothermal agents for bone tumor therapy†

Xin Zhang,[a] Yingzhi Li,[b] Xiaoming Dong,[b] Hao Wang,[b] Bo Chen,[b] Ruiyan Li, [ID] *[b] Yanguo Qin*[b] and Orest Ivasishin[ac]

Large scale bone defects after bone tumor resection are difficult to reconstruct and repair, and there is also the possibility of tumor recurrence. Photothermal therapy (PTT) has the function of inhibiting tumor cells, but the risk of damage to normal cells is the main factor limiting the clinical application of PTT drugs, and most of them have a weak effect on regeneration for bone defects. Therefore, specific biomaterials that simultaneously eliminate bone tumors, have low toxicity, and promote osteogenesis have attracted considerable attention. In this paper, we successfully fabricated bioactive bredigite scaffolds (MS-BRT) functionalized with MoSe$_2$ nanocrystals using a combination of 3D printing and hydrothermal methods. MS-BRT scaffolds not only have low toxicity and good osteogenic ability, but also have the ability to kill bone tumors by photothermal therapy. Using scanning electron microscopy (SEM), X-ray photoelectron spectroscopy (XPS), and an infrared thermal camera, MoSe$_2$ nanocrystals were demonstrated to be successfully modified on the surface of BRT scaffolds. The MoSe$_2$ nanocrystals endow the scaffolds with excellent photothermal properties, which can be well controlled by varying the hydrothermal reaction time and laser power density. Furthermore, the MS-BRT scaffolds can effectively kill MG-63 and HeLa cells and promote the adhesion and proliferation of osteoblasts. The performance of osteoblastic activity was assessed by alkaline phosphatase staining and alizarin red S staining, which results suggest that both MS-BRT and BRT have favorable osteogenic properties. This study combines the photothermal properties of semiconducting MoSe$_2$ nanocrystals with the osteogenic activity of bioceramic scaffolds for the first time, providing a broader perspective for the development of novel biomaterials with dual functions of bone tumor treatment and bone regeneration.

Introduction

Calcium silicate-based ceramic implants are widely used in the reconstruction of large bone defects in bone tissue engineering and clinical practice due to their biocompatibility, biodegradation, and osteoinduction ability. Recent studies have demonstrated that calcium silicate-based ceramics can enhance the proliferation and osteogenic differentiation of bone marrow mesenchymal stem cells and promote angiogenesis by enhancing the *in vitro* and *in vivo* neovascularization of regenerated bone tissue.[1,2] However, large bone defects can be caused by various factors such as osteonecrosis, trauma, bone tumors,

and cancer metastasis. Thus, reconstruction requires not only supporting the bone, but also special treatment for the bone disorder. In particular, for bone defects caused by tumor resection, the reconstruction scaffolds needs to provide structural support and bone ingrowth while also suppressing tumor recurrence.

To achieve good bone support and bone ingrowth, bioceramic implants should have customized shapes and provide structural support to fill the defect area. Three-dimensional (3D) printing, which has emerged as a revolutionary manufacturing technology, has great prospects in a broad range of fields, including bone tissue engineering.[3,4] Various customized porous ceramic scaffolds have been designed and fabricated for bone regeneration using 3D printing techniques.[5–7] In recent studies, 3D porous bioceramic scaffolds have exhibited suitable mechanical strength as bone implant materials and been shown to facilitate the growth of cells and tissues.[8,9]

In the case of bone tumors, an ideal bioceramic implant should include a therapeutic strategy to suppress tumor recurrence. In photothermal therapy (PTT), a non-invasive and non-

[a]Key Laboratory of Automobile Materials of MOE, Department of Materials Science and Engineering, International Center of Future Science, Jilin University, Changchun 130012, China

[b]Department of Orthopedics, The Second Hospital of Jilin University, Jilin University, Changchun 130041, PR China. E-mail: liyandii@msn.cn; qinyg@jlu.edu.cn

[c]G. V. Kurdyumov Institute for Metal Physics, Kyiv, Ukraine

† Electronic supplementary information (ESI) available. See DOI: https://doi.org/10.1039/d2ra02942a

resistant therapeutic treatment that has received widespread attention, near-infrared (NIR) radiation is applied to kill tumor cells.[10] An 808 nm NIR laser can efficiently penetrate through tissues with low tissue absorption.[11] The energy of the absorbed photons is then converted to heat, leading to cell and tissue death at high temperature.[12] Meanwhile, the damage to neighboring healthy tissues can be controlled within a safe range by the simultaneous control of the NIR laser and photothermal conversion agents.[13,14] Currently, carbon nanomaterials,[15–17] two-dimensional (2D) transition metal dichalcogenides (TMDs),[18–21] $Ti_3C_2T_x$ MXene,[22,23] Mxene and gold nanostructures are extensively used as PTT agents for cancer cells *in vitro* and *in vivo*.[24–26] Among them, 2D TMDs have drawn tremendous attention due to their excellent performance in the biomedical field.[27,28] $MoSe_2$ nanoparticles with bandgaps between 1.33 and 1.72 eV are considered as promising PTT agents that exhibit excellent NIR light absorption and high photothermal conversion ability.[29–32] Furthermore, $MoSe_2$ (MS) nanoparticles process lower toxicity compared to other PTT agents because both Mo and Se are necessary trace elements that play active roles in human metabolism.[33–35] Based on these properties, $MoSe_2$ could be applied to functionalize the surfaces of bioceramic scaffolds for PTT, and 3D-printed bioceramic scaffolds functionalized with $MoSe_2$ nanoparticles may be used for both bone regeneration and PTT in the treatment of bone defects caused by bone tumors.

Bredigite ($Ca_7MgSi_4O_{16}$, BRT) is a magnesium silicate-based bioceramic that exhibits rapid hydroxyapatite mineralization, excellent bioactivity, and high osteogenic potential and has a strong stimulating effect on osteoblast proliferation.[36–38] In addition, BRT has a high mechanical strength that is close to that of cortical bone and superior to the mechanical strengths of tricalcium phosphates and other ceramic materials.[39] In this work, for the first time, the surfaces of BRT scaffolds prepared by 3D printing were modified with $MoSe_2$ nanoparticles as photothermal agents using an *in situ* hydrothermal method to form multifunctional scaffolds that possess both anti-tumor and bone repair functions (MS-BRT scaffolds). The structure and composition of the MS-BRT scaffolds were characterized by optical microscopy, scanning electron microscopy (SEM), and X-ray photoelectron spectroscopy (XPS). The MS-BRT scaffolds exhibit considerable bioactivity and excellent photothermal properties, which can effectively cause the death of tumor cells *in vitro*. Thus, the MS-BRT scaffolds show great potential for treating tumor-related bone defects.

Experimental

Materials

Bredigite ($Ca_7MgSi_4O_{16}$, BRT) was purchased from Kunshan Huaqiao New Materials Co., Ltd. Hydroxypropyl methyl cellulose (HPMC) and selenium (Se) were purchased from Aladdin Reagant Co., Ltd. Sodium molybdate ($NaMoO_4 \cdot 2H_2O$) was purchased from Tianjin Fuyu Fine Chemical Co., Ltd. Sodium borohydride ($NaBH_4$) was purchased from Sinopharm Chemical Reagent Co., Ltd. All the chemical reagents were used directly without further purification.

Fabrication of MS-BRT scaffolds

Commercial BRT powders (10 g) were homogeneously mixed with HPMC (6 g, 2 wt%) aqueous solution to produce the ink for printing. The ink was then loaded into a commercial syringe (Nordson EFD, U.S.). Printing was conducted using a direct writing system according to a computer-assisted design model. The final samples were dried at room temperature and then calcined at 1300 °C for 3 h to obtain the BRT scaffolds.

The MS-BRT scaffolds were fabricated using an *in situ* hydrothermal method. Briefly, 1.32 g $Na_2MoO_4 \cdot 2H_2O$, 1.24 g Se powders, and 0.2 g $NaBH_4$ were dissolved in 80 mL of deionized water under vigorous stirring. After 40 min, the mixture was transferred into a Teflon-lined autoclave containing 500 mg of BRT scaffolds and reacted at 200 °C for different times (6, 12, 18, and 24 h). The obtained black scaffolds were collected, washed, and dried at 40 °C under vacuum. The scaffolds prepared with hydrothermal reaction times of 6, 12, 18, and 24 h were marked as 6MS-BRT, 12MS-BRT, 18MS-BRT, and 24MS-BRT, respectively.

Characterizations of MS-BRT scaffolds

Macroscopic photographs of BRT and 12MS-BRT scaffolds were taken using a camera (Nikon). The Zeta potential and particle size of $MoSe_2$ was characterized by a zeta potentiometer (Zetasizer Nano ZS90). The surface morphologies and elemental distributions of the BRT and MS-BRT scaffolds were characterized by SEM (SU8010, Hitachi, Japan) and energy dispersive X-ray spectroscopy (EDS). The chemical compositions of the MS-BRT scaffolds were evaluated by XPS (Escalab-250, Thermo Fisher Scientific, UK). The phase compositions of the scaffolds were determined by X-ray diffraction (D8 Discover, Japan).

Photothermal performance of MS-BRT scaffolds

The photothermal properties of the BRT and MS-BRT scaffolds were investigated by irradiating the scaffolds in quartz cuvettes containing phosphate buffered saline (PBS) with an 808 nm laser for 10 min. The ratio of the scaffolds mass to the PBS volume was controlled to approximately 200 mg mL^{-1}. The temperature of the solution was recorded every 30 s. To regulate the photothermal performance of the MS-BRT scaffolds, the effects of different hydrothermal reaction times and laser power densities were monitored in real time. To detect the thermal stability of the MS-BRT scaffolds, the samples were cyclically irradiated and cooled six times.

Cell attachment and viability

The MC3T3-E1 cells were purchased from the Cell Bank of the YU CAFE Biological Company (Shanghai, China) and cultured in Dulbecco's Modified Eagle Medium (DMEM) containing 10% fetal bovine serum at 37 °C under 5% CO_2. The MC3T3-E1 cells were seeded on the BRT and MS-BRT scaffolds in 24-well plates (2×10^4 cells per well) and cultured for 24 h to observe cell adhesion and cell morphology. The cell-seeded plates were washed with PBS to discard the unattached cells and fixed with 4% paraformaldehyde for 12 min at 4 °C. Cell F-actin was
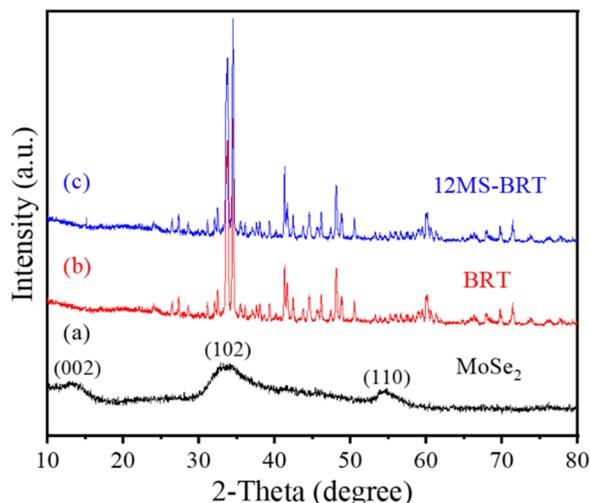
Fig. 1 XRD patterns of (a) MoSe$_2$, (b) BRT and (c) 12MS-BRT scaffold.

stained with phalloidin for 45 min, and the cellular nuclei were stained with 4′,6 diamidino-2-phenylindole (DAPI) for 3–5 min. Rabbit bone marrow mesenchymal stem cells (BMSCs) were harvested by flushing the bone marrow cavities from long bones of 28 day fetal rabbit, and BMSCs between the third and fifth passage were used for testing cytotoxicity and viability. The cytotoxicities of the BRT and MS-BRT scaffolds were further evaluated by culturing BMSCs with the scaffolds in 24-well plates at a cell density of 2×10^4 cells per well for 24 h. Live/dead cell staining kits were used to stain the live and dead cells in different groups using the manufacturer's protocol. The final specimens were observed using a confocal laser scanning microscope (Olympus FV1000, USA). The viabilities of the MC3T3-E1 cells on the surfaces of the BRT and MS-BRT scaffolds were detected using CCK-8 kits after culturing for 24 and 120 h. A mixed solution of DMEM and CCK-8 (DMEM : CCK-8 = 10 : 1) was added into each well followed by incubation at 37 °C for 3 h. The cell viability was then assessed by measuring the optical density at 450 nm using a microplate reader (Varioskan
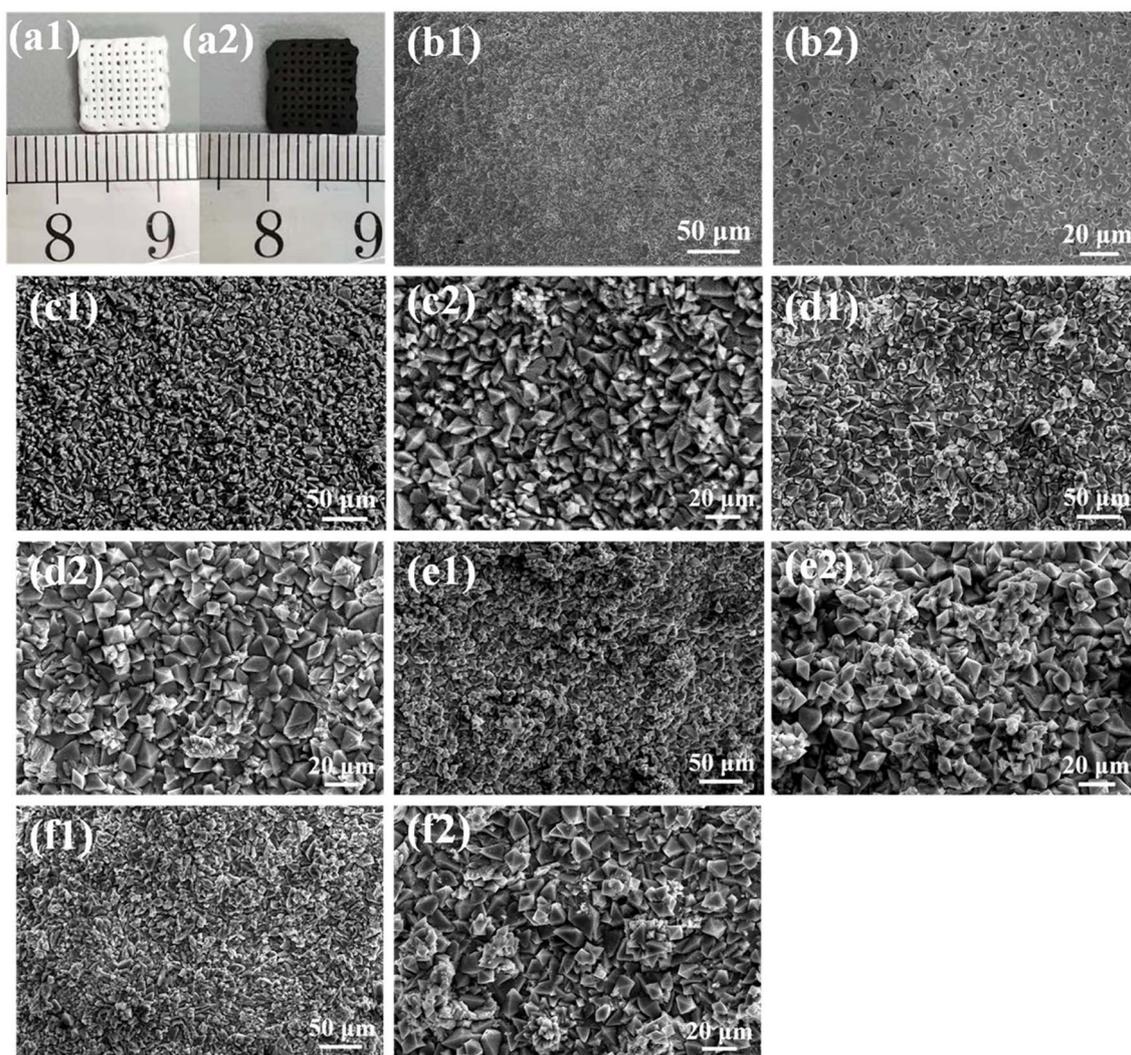

Fig. 2 Photographs of 3D-printed (a1) BRT, (a2) 12MS-BRT scaffolds. SEM images on the pore wall of BRT (b1 and b2), 6MS-BRT (c1 and c2), 12MS-BRT (d1 and d2), 18MS-BRT (e1 and e2), and 24MS-BRT (f1 and f2) scaffolds at different magnification.

Flash, Thermo Scientific) to reflect the proliferation of cells on the BRT and MS-BRT scaffolds.

In vitro anti-tumor efficiency of MS-BRT scaffolds

Tumor cells (MG-63 and HeLa) were purchased from the Cell Bank of the YU CAFE Biological Company (Shanghai, China) and used to evaluate the photothermal effects of the MS-BRT scaffolds. MG-63 and HeLa cells were cultured at densities of 2×10^4 cells per well in different cell wells for 48 h followed by the addition of the BRT and MS-BRT scaffolds into the corresponding cell wells. Subsequently, one group of MG-63 or HeLa cells was irradiated by an NIR laser with a power density of 1.79 W cm^{-2} for 10 min. As a control, the second group was not subjected to laser irradiation. The temperature was recorded using an infrared thermal camera, and the ratio of live to dead cells was determined using live/dead cell staining. The viability of tumor cells was detected using a CCK-8 kit after 12 h. Briefly, the DMEM was removed, and 400 μL of a mixed DMEM/CCK-8 solution (DMEM : CCK-8 = 10 : 1) was added into each well. After incubation for 3 h at 37 °C, the reaction solution was transferred from each well to a new 96-well plate. The absorbance was monitored at 450 nm using a microplate reader (Varioskan Flash, Thermo Scientific).

Cell osteogenic differentiation

The MC3T3-E1 cells were cultured in osteogenic medium (complete medium supplemented with 50 mg L^{-1} ascorbic acid, 10^{-8} M dexamethasone and 10 mM β-glycerol phosphate), and the medium was changed every 2 days. The cell osteogenic differentiation of cells on BRT and 12MS-BRT groups were evaluated by alkaline phosphatase (ALP) staining and alizarin red S (ARS) staining after cultured in osteogenic medium for 4, 7, and 14 days. For ALP staining of the scaffolds, the cells were fixed with 4% paraformaldehyde at 4 °C for 8 min and washed by PBS. ALP staining was measured by an a BCIP/NBT Alkaline Phosphatase Color Development Kit (Beyotime, China) according to the manufacturer's instructions. Then, the zoom stereo microscope was used for observation and imaging. After incubation of 14 days, the MC3T3-E1 cells on the scaffolds were fixed and stained with alizarins kit at room temperature for 40 min in the dark. After washed with PBS several times, the photos were observed under a light microscope. ImageJ was used to get relative mineralization quantification.

Statistical analysis

Each test in this study was replicated at least three times for each group with parallel controls, and the quantitative data were presented as the means ± SD. The statistical analysis among different groups was performed by T tests. P value < 0.05 was considered statistically significant.

Results and discussion

All samples were characterized by X-ray diffraction. Fig. 1a is the XRD pattern of MoSe$_2$ nanocrystals. The sample peaks of the diffraction peaks are obviously broadened, suggesting that the particle size of MoSe$_2$ is nanoscale. The sample has diffraction peaks at $2\theta = 13.3°$, $34.4°$ and $56°$, which can be assigned to the (002), (102) and (110) crystal planes of MoSe$_2$ (JCPDS No. 29-0914).[40] The particle size of MoSe$_2$ was analyzed by DLS nanoparticle analyzer, and the test results showed that the average particle size of MoSe$_2$ was 488 nm, and the zeta potential of the sample measured by dispersing it in water was −24.5 mV, indicating that MoSe$_2$ is unstable in the reaction system and easy to agglomerate, so MoSe$_2$ can be grown *in situ* on the surface of BRT scaffolds, because this can reduce the nucleation barrier of MoSe$_2$ (Fig. S1†). The above results indicate the successful preparation of MoSe$_2$ nanocrystals. The XRD patterns of the BRT scaffolds are shown in Fig. 1b, and the diffraction peaks of the samples correspond one-to-one with the standard card of bredigite (JCPDS No. 36-0399), indicating the successful preparation of the BRT scaffolds, and the samples have large diffraction intensities and narrow half-peak widths,
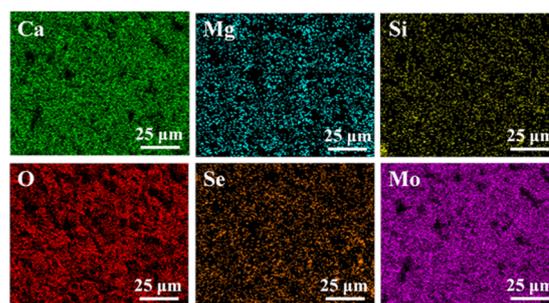

Fig. 3 EDS mapping of Ca, Mg, Si, O, Se, and Mo elements of 12MS-BRT scaffolds.
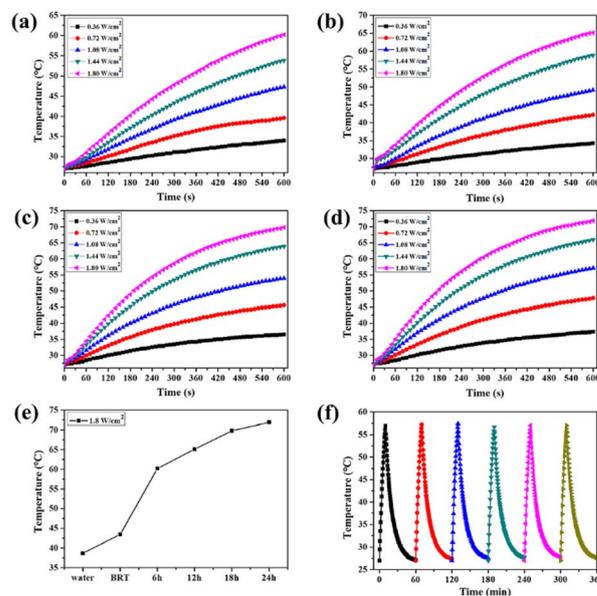

Fig. 4 (a) 6MS-BRT, (b) 12MS-BRT, (c) 18MS-BRT, (d) 24MS-BRT scaffolds heating curve at different laser powers. (e) Temperature rise of different samples after irradiated by 808 nm laser with power density of 1.8 W cm^{-2} for 10 min. (f) Photothermal stability curve of 12MS-BRT scaffolds.

indicating that the BRT scaffolds have excellent crystallinity after high temperature calcination.[41] Fig. 1c is the XRD pattern of the 12MS-BRT scaffolds in which $MoSe_2$ was *in situ* grown on the surface of the BRT scaffolds by the hydrothermal method. It can be seen that there is no obvious difference between the diffraction patterns of the 12MS-BRT scaffolds and the BRT scaffolds. On the one hand, the number of $MoSe_2$ nanocrystals grown *in situ* on the surface of the BRT scaffolds is too small, and on the other hand, the BRT scaffolds after high temperature

calcination has a large diffraction intensity, which masks the characteristic peaks of $MoSe_2$ nanocrystals, so the 12MS-BRT scaffolds has similar XRD patterns to the BRT scaffolds.

Bioactive BRT scaffolds functionalized with $MoSe_2$ nanocrystals as photothermal agents were successfully fabricated using 3D printing technology and *in situ* hydrothermal treatment. The optical photographs of the BRT scaffold and the 12MS-BRT scaffold are shown in Fig. 2a(1) and a(2), respectively. By comparison, it can be seen that the 12MS-BRT scaffold is
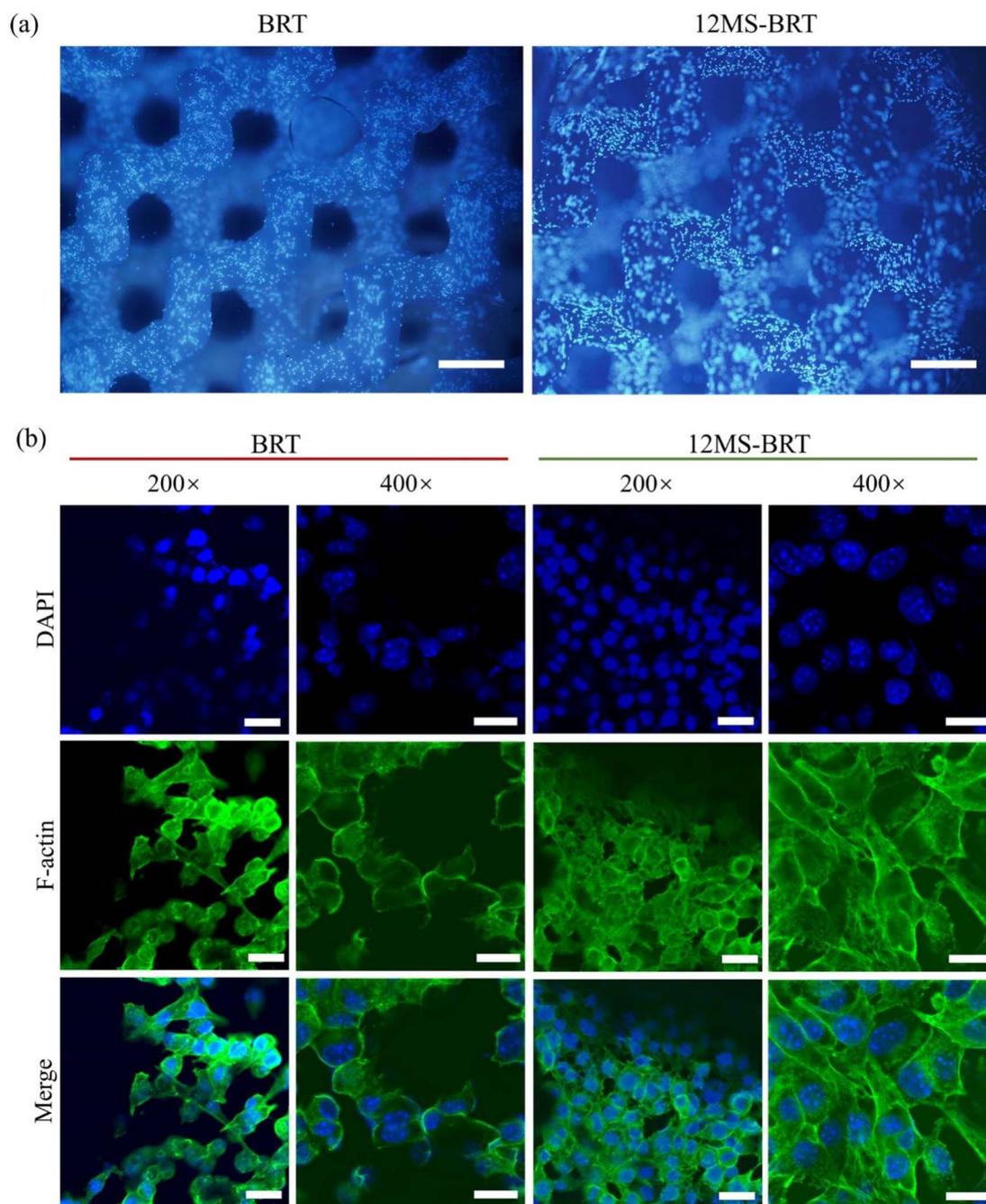

Fig. 5 (a) The fluorescence staining of nucleus of MC3T3-E1 cells on different scaffolds. Scale: 500 μm. (b) The confocal microscopy images of F-actin cytoskeletal morphology for MC3T3-E1 cells (green, phalloidin for F-actin; blue, DAPI for nucleus) after cultured for 24 h. Scale: 200×, 100 μm; 400×, 20 μm.

dark black (Fig. 2a(2)), different from the white color of the BRT scaffold (Fig. 2a(1)). The color change of the scaffolds indicated that MoSe$_2$ nanocrystals were successfully grown *in situ* on the surface of the BRT scaffolds through hydrothermal reaction, and the successful modification of MoSe$_2$ nanocrystals was the premise of using photothermal therapy to kill bone tumors. The SEM of the BRT scaffolds is shown in Fig. 2b, the BRT scaffolds has a relatively dense and smooth surface (Fig. 2b(1) and b(2)), but a large number of holes exist on the surface of the scaffolds, which is a typical morphology of ceramic samples synthesized by high temperature calcination. The SEM images of MS-BRT scaffolds at different times of hydrothermal reaction are shown in Fig. 2c–f, respectively. And by further prolonging the hydrothermal time, the MoSe$_2$ nanocrystals agglomerated and grew into large particles on the surface of the BRT scaffolds, resulting in an increase in the content of MoSe$_2$ nanocrystals on the surface of the BRT scaffolds, which would further enhance the photothermal capability of the BRT scaffolds.

Fig. 3 shows the EDS mapping of Ca, Si, Mg, O, Mo, and Se elements on the surface of the 12MS-BRT scaffolds. All these elements are uniformly distributed on the strut surface of the 12MS-BRT scaffolds, further indicating the homogeneity of the material and the successful preparation of the sample. The characteristic peaks of Mo and Se were also detected by XPS, as shown in Fig. S2.† The peaks at 55.4 eV and 54.5 eV can be assigned to Se 3d$_{3/2}$ and Se 3d$_{5/2}$, respectively, indicating that Se is in the −2 oxidation state.[42] The binding energies of Mo 3d$_{3/2}$ and Mo 3d$_{5/2}$ are 235.2 eV and 232.0 eV, respectively, indicating that Mo is in the +6 oxidation state.[43] On the one hand, the appearance of Mo^{6+} is because XPS can only characterize the information at the depth of 3–10 nm on the surface. On the other hand, because Mo^{6+} is more stable than Mo^{4+}, the Mo^{4+} on the surface of the BRT scaffolds is further oxidized to Mo^{6+} under the high temperature and high pressure environment inside the reactor. We speculate that Mo^{6+} exists in the form of a trace amount of MoO$_3$. It is known from the work of others that the forbidden bandwidth of MoO$_3$ is slightly less than 3 eV, so MoO$_3$ does not have good photothermal conversion ability.[44,45] However, from the following photothermal properties test of the scaffolds, we know that the MS-BRT scaffolds prepared by us has good conversion ability, so a large number of materials grown *in situ* on the surface of the scaffolds are MoSe$_2$.

The photothermal properties of MS-BRT scaffolds irradiated with 808 nm laser in PBS for hydrothermal reactions for different times were investigated, as shown in Fig. 4a–e. As the laser power density increased from 0.36 W cm^{-2} to 1.80 W cm^{-2}, the PBS temperature of MS-BRT scaffolds with different hydrothermal reaction times all increased significantly. With the increase of irradiation time, the solution temperature first increased and then tended to be stable. At a laser power density of 1.80 W cm^{-2}, the final temperatures reached 62 °C (6MS-BRT), 65 °C (12MS-BRT), 70 °C (18MS-BRT) and 73 °C (24MS-BRT), respectively. Under the same laser power density, the temperature of PBS equipped with MS-BRT scaffolds with different hydrothermal reaction times gradually increased. This is because with the prolongation of the

hydrothermal reaction time, the content of MoSe$_2$ on the surface of the scaffolds increases, so the photothermal performance is further improved, which is consistent with the results of SEM characterization. In contrast, under the same conditions, the temperature of the BRT scaffolds and pure water increased slightly, which can be attributed to the slight absorption of NIR energy by water, and the unmodified BRT scaffolds and pure water had no obvious photothermal properties (Fig. S3†). The photothermal stability of the 12MS-BRT scaffolds was also evaluated by monitoring the temperature during laser on/off cycling. The photothermal effect of the 12MS-BRT scaffolds did not decrease after 6 cycles, confirming the stability of the 12MS-BRT scaffolds as a photothermal agent (Fig. 4f). These results suggest that MS-BRT scaffolds are excellent photothermal materials that can be used for PTT.

This paper is the first to report the study of photothermal therapy by *in situ* growth of MoSe$_2$ on the surface of BRT scaffold by hydrothermal method, it was impossible to compare the photothermal properties with the papers published by the peers, so we chose MoS$_2$, which is similar in chemical composition to MoSe$_2$ and also has photothermal properties for comparison. In the work of Wu *et al.*, MoS$_2$ was grown *in situ* on the surface of akermanite scaffolds, and photothermal characterization was performed by adding 500 μL PBS to create a humid environment, the laser power density was 0.5 W cm^{-2}, and the temperature reached 50 °C after 10 min.[46] In the work of Li *et al.*, MoS$_2$ was grown *in situ* on the surface of bioactive glass scaffolds, the scaffolds were immersed in pure water, the laser power density was 2 W cm^{-2}, and the temperature of the scaffolds was 53 °C after 8 min.[47] In this paper, the fabricated samples were completely immersed in PBS, the laser power density was 1.8 W cm^{-2}, and after 8 min irradiation, the temperature of the scaffolds with different time hydrothermal
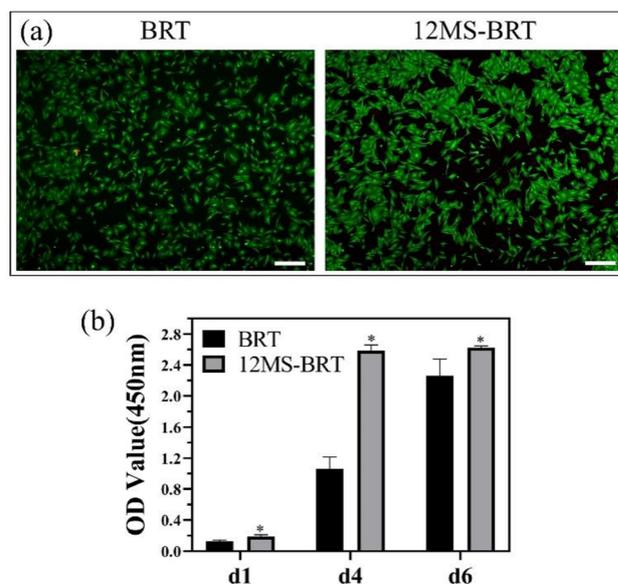

Fig. 6 (a) Images of live/dead cells staining of BMSCs on BRT and 12MS-BRT scaffolds. Scale: 100 μm. (b) Cell proliferation of MC3T3-E1 cells on different samples after culture for 1, 4, and 6 days.
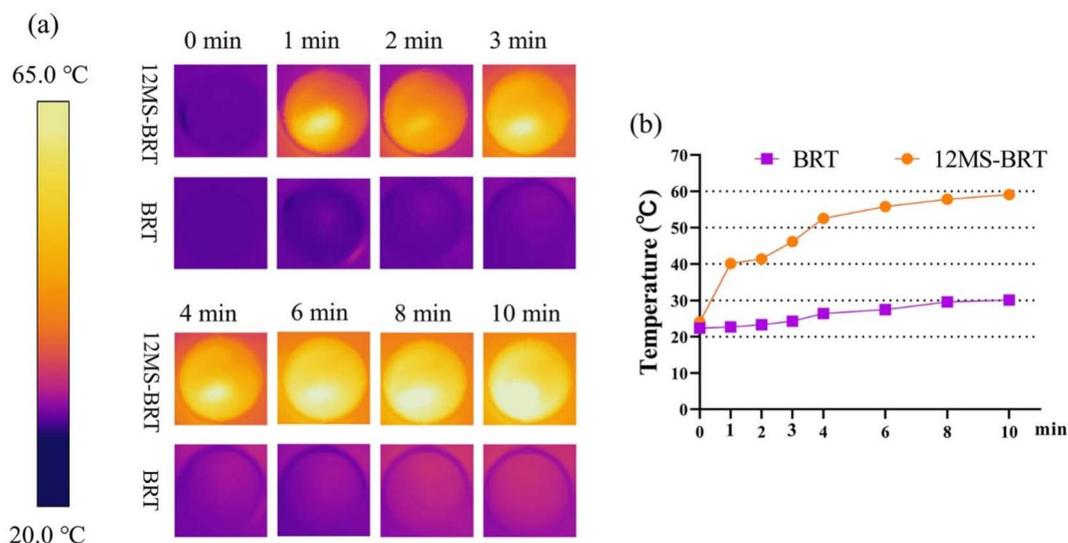
Fig. 7 Thermal images (a) and heating curves (b) of BRT and 12MS-BRT scaffolds with 808 nm laser irradiation.

reactions was at least 55 °C, which proved that the samples prepared by us had excellent photothermal conversion ability. And compared with the S element, the Se element has more advantages in osteogenesis, so we estimate that the BRT scaffolds modified *in situ* by MoSe$_2$ will have a better performance in promoting the adhesion and proliferation of osteoblasts.
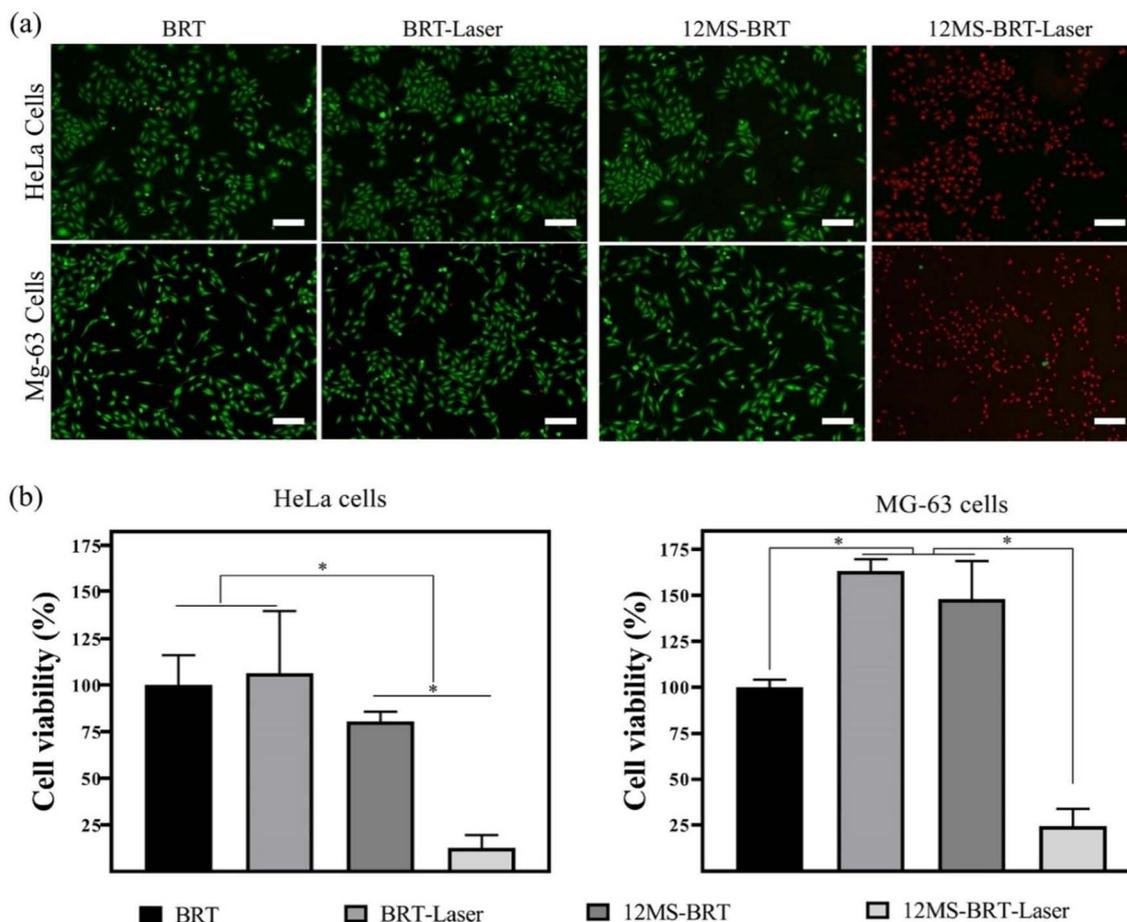

Fig. 8 (a) Fluorescent images of live and dead cells on BRT and 12MS-BRT scaffolds after laser irradiation and without laser irradiation, scale: 200 μm. (b) The quantification of cell viability for HeLa and MG-63 cells after laser irradiation for 12 h and without laser irradiation.

The adhesion and morphology of MC3T3-E1 cells on the BRT and 12MS-BRT scaffolds after culturing for 24 h were observed by fluorescence microscopy (Fig. 5a) and laser scanning confocal microscopy (Fig. 5b). Many cells were adhered on the pore walls of the BRT and 12MS-BRT scaffolds. The confocal laser scanning microscopy images show that most of the cells on the BRT scaffolds exhibited round and shrink shapes after seeding for 24 h. In contrast, the cells on the 12MS-BRT scaffolds showed typical spindle stem cell morphologies with clear cell microfilaments, indicating that the incorporation of MoSe$_2$ onto BRT was favorable for cell adhesion. Similar results were obtained for the adhesion and morphology of BMSCs (Fig. S4†). The cell cytotoxicities on the BRT and 12MS-BRT scaffolds were also analyzed via live/dead cell staining. As shown in Fig. 6a, the BMSCs exhibited green fluorescence, which indicates live cells, after co-culturing with the BRT or 12MS-BRT scaffolds for 24 h. Thus, the BRT and 12MS-BRT scaffolds showed negligible cytotoxicity to BMSCs. The viabilities of MC3T3-E1 cells on the BRT and 12MS-BRT scaffolds were monitored after culturing for 24 and 120 h by CCK-8 assay (Fig. 6b). The number of MC3T3-E1 cells increased with culture time on both the BRT and 12MS-BRT scaffolds; however, the cell proliferation rate was much higher on the 12MS-BRT scaffolds than on the BRT scaffolds at both time points. These results indicate that the BRT and 12MS-BRT scaffolds did not inhibit the growth of MC3T3-E1 cells.

To evaluate scaffolds degradation, the BRT and 12MS-BRT scaffolds were soaked in simulated body fluid (SBF) for 14 d at 37 °C. The degradation rates of the BRT and 12MS-BRT scaffolds were approximately 68% and 47%, respectively (Fig. S4†). These results demonstrate that the 12MS-BRT scaffolds have excellent biodegradability and high biocompatibility, making it suitable for use in bone reconstruction. The excellent biocompatibility can be attributed to the functional elements in the scaffolds, which enhance the bioactivity of the interface between the scaffolds and cells. Furthermore, the functional elements can be released from the scaffolds (Fig. S5†), which would improve the microenvironment for bone healing.

To analyze the photothermal effects of the BRT and 12MS-BRT scaffolds, the changes in temperature were recorded by an infrared thermal camera (Fig. 7). The corresponding infrared thermal images show that the temperature of DMEM containing 12MS-BRT rapidly increased to the equilibrium temperature of 59.1 °C under NIR laser irradiation for 10 min. In striking contrast, the temperature of DMEM containing the BRT scaffolds increased only slightly from 21 °C to approximately 30 °C after laser irradiation for 10 min. These results suggest that the 12MS-BRT scaffolds possesses excellent photothermal performance and can be used for PTT.

Inspired by the excellent photothermal performance of the 12MS-BRT scaffolds, we further investigated the photothermal anti-tumor effect of the 12MS-BRT scaffolds in vitro. MG-63 and HeLa cells were incubated with the BRT and 12MS-BRT scaffolds and irradiated using an 808 nm laser (Fig. 8). Almost all the cells on the BRT scaffolds showed green fluorescence both with and without laser irradiation, implying the hypotoxicity of BRT and the laser irradiation to tumor cells. In contrast, the cells on the 12MS-BRT scaffolds exhibited red fluorescence

(indicative of dead cells) after laser irradiation for 10 min. The cells on the 12MS-BRT scaffolds showed green fluorescence before laser irradiation, indicating that the enhanced cytotoxicity was derived from the PTT effect of MoSe$_2$. Subsequently, the cell viabilities of HeLa and MG-63 cells were evaluated. No reduction in cell viability on the BRT scaffolds was observed with or without laser irradiation. In contrast, the tumor cells on the 12MS-BRT scaffolds showed an obvious reduction in cell viability after laser irradiation, consistent with the results of live/dead cell staining. Collectively, these results indicate that the 12MS-BRT scaffolds have an obvious anti-tumor cell effect resulting from the photothermal effect of MoSe$_2$.

When the residual tumor tissue is eliminated, the effect of bone regeneration becomes the main requirement of the scaffolds in the next stage. The pro-osteogenic performance of BRT
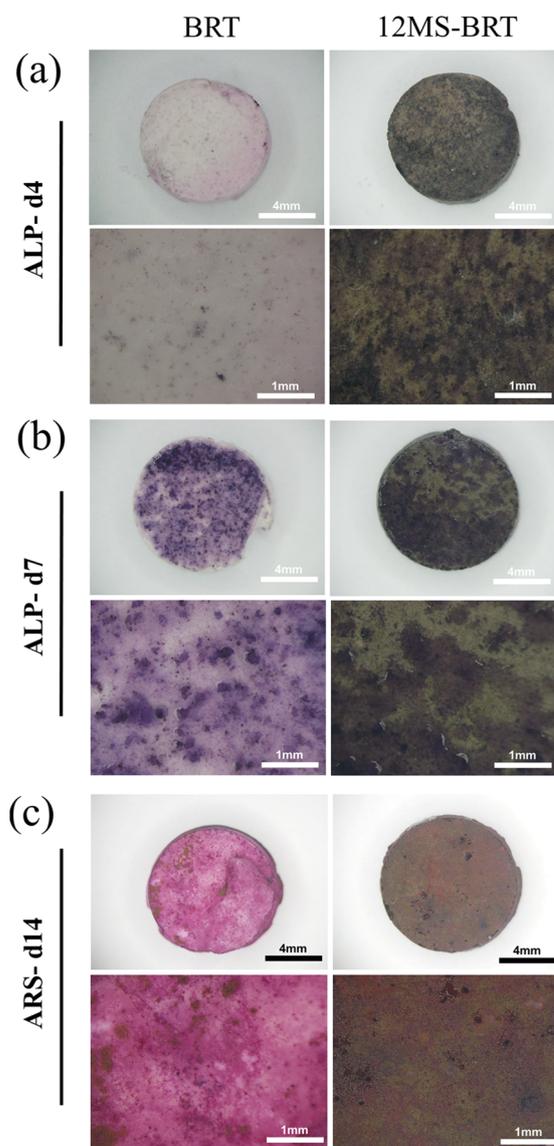

Fig. 9 The photographs of ALP staining for BRT and 12MS-BRT scaffolds at 4 days (a) and 7 days (b), the photographs of ARS staining for BRT and 12MS-BRT at 14 days (c).

and 12MS-BRT groups were evaluated by alkaline phosphatase (ALP) staining and alizarin red S (ARS) staining. As shown in the Fig. 9a and b, after 4 and 7 days of osteogenic induction, there were many blue-purple stained areas on the surface of the two groups of samples. Compared with BRT group, the 12MS-BRT group showed much more ALP-positive areas at 4 days, indicating that 12MS-BRT enhanced the early secretion of ALP for MC3T3-E1 cells. The images of ARS staining for 14 days were shown in the Fig. 9c, there are numerous red-stained calcium nodules deposited on both the BRT and 12MS-BRT groups, while the larger area of calcium nodules emerge on the BRT group. The relative mineralization quantification (Fig. S7†) of different groups at 14 days also showed that the number of calcium nodules of the BRT group was higher than the 12WS-BRT group. These results indicate that BRT and 12MS-BRT groups could enhance the ability of osteogenic differentiation, and the surface for BRT is more suitable for mineralization. The ability of osteogenic differentiation may be related to functional elements such as calcium, silicon, and magnesium contained in bredigite ($Ca_7MgSi_4O_{16}$).

Conclusions

In conclusion, in this study MS-BRT scaffolds were fabricated by combining 3D printing with in situ hydrothermal treatment to in situ grow $MoSe_2$ nanocrystals on the surface of BRT scaffolds. Due to the $MoSe_2$ nanocrystals on the surface, the obtained scaffolds exhibited excellent photothermal properties and could be effectively controlled by changing the hydrothermal reaction time and laser power density. The high temperature generated by the 12MS-BRT scaffolds prepared under near-infrared light irradiation could effectively kill tumor cells in vitro, and the 12MS-BRT scaffolds showed good biosafety and osteopromoting activity. Both MS-BRT and BRT have favorable osteogenic properties. Furthermore, the MS-BRT scaffolds possess the ability to kill MG-63 and HeLa cells and regenerate bone defect. Therefore, such a bifunctional scaffolds integrating tumor therapy with bone regeneration could provide a promising clinical therapy strategy for therapy of tumor-induced bone defects.

Conflicts of interest

The authors declare that the research was conducted in the absence of any commercial or financial relationships that could be construed as a potential conflict of interest.

Acknowledgements

Notes and references

1 S. J. Ding, M. Y. Shie, T. Hoshiba, N. Kawazoe, G. P. Chen and H. C. Chang, *Tissue Eng., Part A*, 2010, **16**, 2343–2354.

2 W. Y. Zhai, H. X. Lu, L. Chen, X. T. Lin, Y. Huang, K. R. Dai, K. Naoki, G. P. Chen and J. Chang, *Acta Biomater.*, 2012, **8**, 341–349.

3 B. Baumann, T. Jungst, S. Stichler, S. Feineis, O. Wiltschka, M. Kuhlmann, M. Linden and J. Groll, *Angew. Chem., Int. Ed.*, 2017, **56**, 4623–4628.

4 A. Khademhosseini and R. Langer, *Nat. Protoc.*, 2016, **11**, 1775–1781.

5 Y. L. Zhang, D. Zhai, M. C. Xu, Q. Q. Yao, H. Y. Zhu, J. Chang and C. T. Wu, *Biofabrication*, 2017, **9**, 11.

6 W. L. Shi, M. Y. Sun, X. Q. Hu, B. Ren, J. Cheng, C. X. Li, X. N. Duan, X. Fu, J. Y. Zhang, H. F. Chen and Y. F. Ao, *Adv. Mater.*, 2017, **29**, 7.

7 I. Sabree, J. E. Gough and B. Derby, *Ceram. Int.*, 2015, **41**, 8425–8432.

8 R. Wang, P. F. Zhu, W. Y. Yang, S. Gao, B. Li and Q. Li, *Mater. Des.*, 2018, **144**, 304–309.

9 W. Yu, X. Sun, H. Y. Meng, B. C. Sun, P. Chen, X. J. Liu, K. H. Zhang, X. Yang, J. Peng and S. B. Lu, *Biomater. Sci.*, 2017, **5**, 1690–1698.

10 H. Lin, Y. Chen and J. L. Shi, *Chem. Soc. Rev.*, 2018, **47**, 1938–1958.

11 S. Wu and H. J. Butt, *Adv. Mater.*, 2016, **28**, 1208–1226.

12 H. Lin, Y. W. Wang, S. S. Gao, Y. Chen and J. L. Shi, *Adv. Mater.*, 2018, **30**, 11.

13 Y. J. Liu, P. Bhattarai, Z. F. Dai and X. Y. Chen, *Chem. Soc. Rev.*, 2019, **48**, 2053–2108.

14 L. Cheng, C. Wang, L. Z. Feng, K. Yang and Z. Liu, *Chem. Rev.*, 2014, **114**, 10869–10939.

15 J. C. Ge, Q. Y. Jia, W. M. Liu, M. H. Lan, B. J. Zhou, L. Guo, H. Y. Zhou, H. Y. Zhang, Y. Wang, Y. Gu, X. M. Meng and P. F. Wang, *Adv. Healthcare Mater.*, 2016, **5**, 665–675.

16 H. K. Moon, S. H. Lee and H. C. Choi, *ACS Nano*, 2009, **3**, 3707–3713.

17 X. W. Liu, H. Q. Tao, K. Yang, S. A. Zhang, S. T. Lee and Z. A. Liu, *Biomaterials*, 2011, **32**, 144–151.

18 L. Cheng, J. J. Liu, X. Gu, H. Gong, X. Z. Shi, T. Liu, C. Wang, X. Y. Wang, G. Liu, H. Y. Xing, W. B. Bu, B. Q. Sun and Z. Liu, *Adv. Mater.*, 2014, **26**, 1886–1893.

19 N. Ma, M. K. Zhang, X. S. Wang, L. Zhang, J. Feng and X. Z. Zhang, *Adv. Funct. Mater.*, 2018, **28**, 11.

20 T. Liu, C. Wang, X. Gu, H. Gong, L. Cheng, X. Z. Shi, L. Z. Feng, B. Q. Sun and Z. Liu, *Adv. Mater.*, 2014, **26**, 3433–3440.

21 H. Ma and M. A. Q. Xue, *J. Mater. Chem. A*, 2021, **9**, 17569–17591.

22 H. Ma, H. G. Cheng, X. L. Ma, S. Wang, Z. Q. Zhou, Y. Q. Chai, R. Q. Chen, X. Y. Zhang, Y. L. He, Y. P. Wang, Y. Li, X. S. Wang, R. Li, N. Ma and M. Q. Xue, *J. Mater. Chem. A*, 2020, **8**, 19022–19027.

23 H. Lin, Y. Chen and J. L. Shi, *Adv. Sci.*, 2018, **5**, 20.

24 J. S. Han, J. J. Zhang, M. Yang, D. X. Cui and J. M. de la Fuente, *Nanoscale*, 2016, **8**, 492–499.

25 Y. L. Liu, M. Yang, J. P. Zhang, X. Zhi, C. Li, C. L. Zhang, F. Pan, K. Wang, Y. M. Yang, J. M. de la Fuentea and D. X. Cui, *ACS Nano*, 2016, **10**, 2375–2385.

26 J. L. Li, D. Day and M. Gu, *Adv. Mater.*, 2008, **20**, 3866–3871.

27 Y. Yong, X. J. Cheng, T. Bao, M. Zu, L. Yan, W. Y. Yin, C. C. Ge, D. L. Wang, Z. J. Gu and Y. L. Zhao, *ACS Nano*, 2015, **9**, 12451–12463.

28 H. Chen, T. J. Liu, Z. Q. Su, L. Shang and G. Wei, *Nanoscale Horiz.*, 2018, **3**, 74–89.

29 Y. Li, R. Jia, H. M. Lin, X. L. Sun and F. Y. Qu, *Adv. Funct. Mater.*, 2021, **31**, 13.

30 C. Wang, J. Bai, Y. W. Liu, X. D. Jia and X. Jiang, *ACS Biomater. Sci. Eng.*, 2016, **2**, 2011–2017.

31 Y. Wang, F. Zhang, Q. Wang, P. P. Yang, H. M. Lin and F. Y. Qu, *Nanoscale*, 2018, **10**, 14534–14545.

32 Y. Wang, J. X. Zhao, Z. Chen, F. Zhang, W. Guo, H. M. Lin and F. Y. Qu, *Appl. Catal., B*, 2019, **244**, 76–86.

33 M. Ryan-Harshman and W. Aldoori, *Can. J. Diet. Pract. Res.*, 2005, **66**, 98–102.

34 R. Boyd, *Nat. Chem.*, 2011, **3**, 570.

35 R. Vilar, *Transition Met. Chem.*, 2012, **37**, 605–606.

36 W. Y. Zhai, H. X. Lu, C. T. Wu, L. Chen, X. T. Lin, K. Naoki, G. P. Chen and J. Chang, *Acta Biomater.*, 2013, **9**, 8004–8014.

37 C. T. Wu, J. A. Chang, J. Y. Wang, S. Y. Ni and W. Y. Zhai, *Biomaterials*, 2005, **26**, 2925–2931.

38 C. Wu and J. Chang, *J. Biomed. Mater. Res., Part B*, 2007, **83B**, 153–160.

39 P. Srinath, P. A. Azeem and K. V. Reddy, *Int. J. Appl. Ceram. Technol.*, 2020, **17**, 2450–2464.

40 S. K. Balasingam, J. S. Lee and Y. Jun, *Dalton Trans.*, 2015, **44**, 15491–15498.

41 M. Rahmati, M. Fathi and M. Ahmadian, *J. Alloys Compd.*, 2018, **732**, 9–15.

42 H. Tang, H. Huang, X. S. Wang, K. Q. Wu, G. G. Tang and C. S. Li, *Appl. Surf. Sci.*, 2016, **379**, 296–303.

43 C. Y. Wu, Z. L. Liu, Z. X. Chen, D. L. Xu, L. S. Chen, H. Lin and J. L. Shi, *Sci. Adv.*, 2021, **7**, 11.

44 A. Fakhri and P. A. Nejad, *J. Photochem. Photobiol., B*, 2016, **159**, 211–217.

45 H. M. Hu, C. H. Deng, J. C. Xu, K. H. Zhang and M. Sun, *J. Exp. Nanosci.*, 2015, **10**, 1336–1346.

46 X. C. Wang, T. Li, H. S. Ma, D. Zhai, C. Jiang, J. Chang, J. W. Wang and C. T. Wu, *NPG Asia Mater.*, 2017, **9**, 14.

47 H. Wang, X. Q. Zeng, L. B. Pang, H. H. Wang, B. C. Lin, Z. W. Deng, E. L. X. Qi, N. Miao, D. P. Wang, P. Huang, H. R. Hu and J. S. Li, *Chem. Eng. J.*, 2020, **396**, 14.